Aerodynamic Characterisation of Communicating Turbulent Boundary Layers Through a Porous Medium Subjected to a Pressure Differential

Aeroacoustics Conferences
June 4-7, 2024, Rome, Italy
30th AIAA/CEAS Aeroacoustics Conference (2024)

10.2514/6.2024-3049

Aerodynamic characterisation of communicating turbulent boundary layers through porous media subjected to a pressure differential

Thomas P. Hunter*
Delft University of Technology, Delft, The Netherlands

Francesco Avallone†
Politecnico de Torino, Torino, Italy

Anh Khoa Doan‡ and Daniele Ragni§
Delft University of Technology, Delft, The Netherlands

Permeable materials are a promising trailing edge noise reduction technique. The noise reduction is a result of the unsteady interaction between the two communicating boundary layers, in a process referred to as the pressure release mechanism. However, in practice the aeroacoustic performance of permeable trailing edges degrades under lifting conditions, i.e. with a pressure and velocity differential. This study aims at investigating such flow physics using the Lattice Boltzmann Method through 3DS PowerFLOW. A numerical setup was created to explore the impact of velocity and pressure differentials between two communicating boundary layers and relate them to the aeroacoustic performance of porous media. The proposed numerical setup consists of two vertically stacked temporally developing channel flows separated by a porous medium $(6\delta \times (4\delta + t) \times 2\delta)$**, where** δ **and** t **are the half-channel height and the porous medium thickness respectively. The two channel flows communicate through fully resolved porous media, here, 75% porous triply periodic minimal surfaces. A large drag increase is observed for all geometries. An increase in anti-correlation between the pressure fluctuations between the channels is found to be related to a drag increase. It was concluded that the spanwise coherent turbulent structures drive the increase in drag. These structures are also affected by the geometry of the porous medium at the surface of the grazing flows. The presence of large coherent turbulent structures leads to a shift in turbulent energy scales. This is related to the modification of the wall pressure spectrum, where it was observed that less energy is present at low frequencies, whereas a peak was observed at a higher frequency. The crossover frequency is between** $150Hz$ **and** $600Hz$**.**

I. Introduction

Trailing edge noise can be mitigated by various means, such as trailing edge serrations [1]. In recent times, porous trailing edges were considered due to their large noise reduction potential with respect to state-of-the-art serrations [2]. The larger noise reduction potential (about 4dB for the serrations [3] and 10dB for the porous trailing edges [4]) is coupled to the potential of noise reduction in a wider range of operating conditions. However, similarly to serrated trailing edges, the noise reduction potential reduces under loading [5, 6]. Porous media also result in a high frequency acoustic signature, attributed to the impact of roughness [7]. By enabling a hydrodynamic communication between pressure and suction side of the airfoil, a porous trailing edge provides a milder transition between solid airfoil and the wake [8]. The communication between the two boundary layers was quickly identified as a necessary condition and the largest driver for the noise reduction [8].

The noise reduction process of porous trailing edges has been studied both numerically [9] and experimentally [10]. The main material property related to the noise reduction potential of porous media was identified to be its permeability,

*Doctoral Candidate, Aerodynamics Department, t.p.hunter@tudelft.nl, Delft 2629HS, The Netherlands. AIAA Student Member
†Professor, Department of Mechanical and Aerospace Engineering, Torino 10129, Italy. AIAA Member
‡Assistant Professor, Aerodynamics Department, Delft 2629HS, The Netherlands. AIAA Member
§Associate Professor, Wind Energy Department, Delft 2629HS, The Netherlands. AIAA Member

although tortuosity [10] and Forchheimer term [11] were also reported to have an impact on the acoustic signature of permeable trailing edges. The inability to consistently relate topological parameters to material properties highlights the need for a novel approach to generate, characterise and model porous media in the context of communicating grazing flows.

Numerical investigations enabled the reconstruction of the internal hydrodynamic field of the porous medium. Ref. [12] identified the ability of porous trailing edges to enable the communication between pressure fluctuations on both sides of the airfoil at lower frequencies. This was observed to lead to a shift in turbulent kinetic energy spectrum to higher frequencies, which are scattered less efficiently. Additionally, other studies highlighted the impact of the non-linear effects of the porous trailing edges for the noise reduction [11, 13].

The non-linear permeability parameter has also been associated to the increase in drag in the context of turbulent flows above acoustic liners [14]; it should be noted that this medium is unidirectionally permeable. The noise reduction is therefore also associated to an aerodynamic penalty [6]. The effect of porous walls on drag has been independently studied in past research mostly using the Turbulent Channel Flow (TCF) configuration [15–17] and, in this context, porous walls are related to a lower friction coefficient since they allow for the creation of a slip velocity at the location where the solid wall would be. This comes at the cost of pressure drag which is significant and has been shown to contribute 40 to 400% of drag in acoustic liners [18]. The study of acoustic liners related the drag increase to the inverse of the non-linear permeability $1/C^+$ [19]. This was found by observing that the previously used criterion of the square root of the permeability $\sqrt{K^+}$ showed a non-monotonic behaviour for the acoustic liners.

Moreover, choosing ill-suited material properties also results in undesirable aeroacoustic performance. In the case presented in Ref. [11], the permeability is increased to attempt to maximise the noise reduction potential. However, the non-linear permeability term is modified through the application of a liner on the porous trailing edge. This resulted in strong tonal noise despite the noise reduction in overall sound pressure level. The onset of this behaviour cannot presently be predicted.

Therefore, the relationship between the communication of boundary layers and aeroacoustic performance of porous trailing edges remains largely unexplored. We propose and use a dedicated numerical setup, based on turbulent channel flows communicating through fully resolved porous media. The definition of the porous media is provided analytically and different inflow conditions can be imposed in the channels. The setup focuses on how the flow communication through the flow permeable material modifies the boundary layer on both sides with respect to the smooth non-permeable wall.

The goal of this study consists therefore in exploring the aerodynamic performance of communicating grazing flows through porous media subjected to a pressure differential and relate it to material properties.

This paper is structured as follows. In section II, the numerical setup and the verification procedure will be presented. First the geometries of the porous media of interest are presented, as well as the method used to characterise them. This is followed by a grid convergence study as well as an analysis related to the sizing of the domain. In section III, the results are presented in two subsections. The first focuses on the additional drag imparted on the channels based on the flow conditions. The second subsection analyses the wall pressure spectrum at the surface of the porous medium. The last results subsection presents a comparison of the aerodynamic performance to material properties. Finally, section IV presents the conclusions of this paper.

II. Numerical setup

Our proposed setup, illustrated in Figure 1 consists in two vertically stacked turbulent channel flows communicating through a porous medium. This allows to study the effect of variations in the porous medium design space (i.e. scale, porosity, thickness, etc.) and flow conditions (streamwise and wall-normal pressure gradients) on the aerodynamic performance of the considered porous flat plate.

Periodic boundary conditions are applied in the stream- and spanwise directions, and the top and bottom channels are bound by the porous medium on one side and a smooth non-slip wall on the other. The flow is driven by a local forcing term, analogous to a pressure gradient in the streamwise direction, $\mathrm{d}p/\mathrm{d}x$. Variations in the forcing term applied to each channel result in differing bulk velocities, based on the drag present in the channels.

The choice of porous medium for this study was performed by identifying a porous medium design space sufficiently topologically complex and easily described by a few parameters. These criteria were chosen in order to emulate similar properties to the metal foams whose noise reduction was documented [5, 10]. The chosen design space is composed of the triply periodic minimal surfaces (TPMS). These surfaces are defined as minimising the surface area enclosed by a

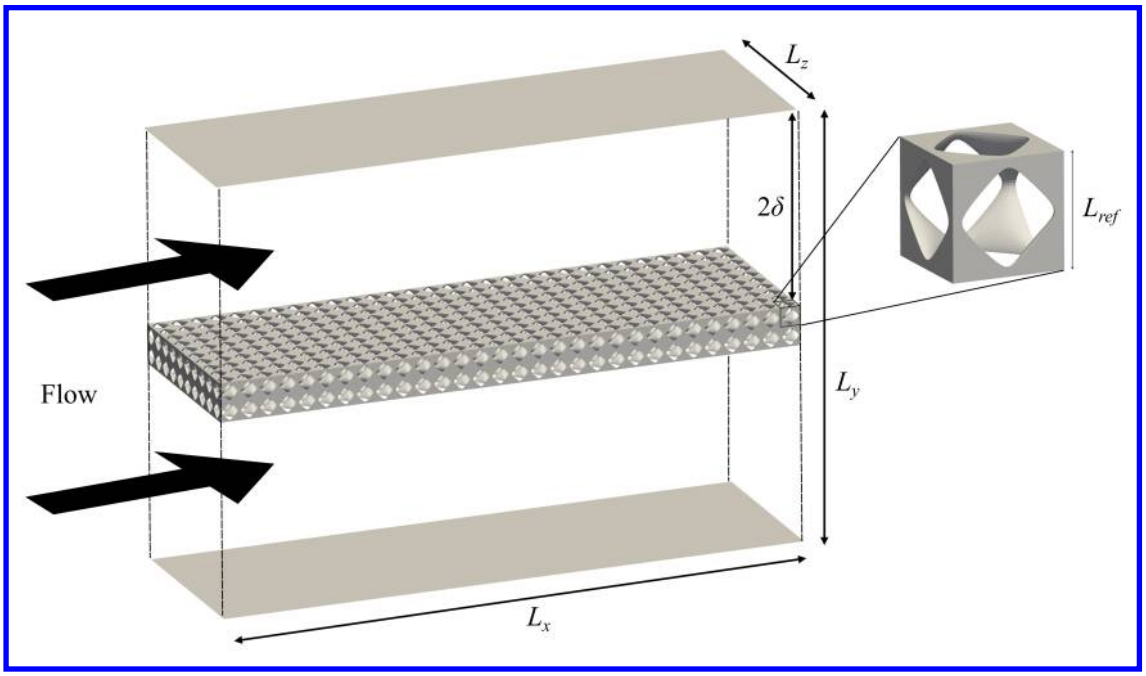

Fig. 1 Schematic of the proposed Communicating Turbulent Channel Flows (C-TCF) and unit cell of the 75% porous TPMS Schwarz's P "Primitive"

curve [20]. Specifically, the subset of TPMS of interest are obtained through the following explicit relations:

$$\begin{aligned} x_1 &= \Lambda_1 Re\left(e^{i\theta}\int_{\omega_0}^{\omega}(1-\tau^2)R(\tau)\,d\tau\right) \\ x_2 &= \Lambda_2 Re\left(e^{i\theta}\int_{\omega_0}^{\omega} i(1+\tau^2)R(\tau)\,d\tau\right) \\ x_3 &= \Lambda_3 Re\left(e^{i\theta}\int_{\omega_0}^{\omega} 2\tau R(\tau)\,d\tau\right), \end{aligned} \tag{1}$$

where $i = -1^2$, Λ_i the anisotropy vector, and $\tau = \tau_a + i\tau_b$, associating with the Weierstrass function $R(\tau) = \frac{1}{\sqrt{\tau^8+\lambda\tau^4+1}}$, θ the Bonnet angle and $\lambda = -14$. This Weierstrass function enables the creation of a TPMS family that is described by its Bonnet angle and Λ_i. The coordinates are obtained by evaluating the real part ($Re(\cdot)$) of the integrals from some fixed points ω_0 to a variable point ω in the complex plane. The surface, thus obtained, can be assembled to form a triply periodic surface [21]. The three Bonnet angles for which the surfaces are not self-intersecting are 0, $acot(EllipticK[1/4]/EllipticK[3/4])$, and $\pi/2$ [22].

These surfaces can be approximated by the periodic nodal surface of a sum defined in terms of a Fourier series [22].

$$\phi(\mathbf{r}) = \sum_{\mathbf{k}} F(\mathbf{k})\cos\pi\mathbf{k}\cdot\mathbf{r} - \alpha(\mathbf{k})] = 0 \tag{2}$$

where $\mathbf{k}$ are the reciprocal lattice vectors, $\alpha(\mathbf{k}$, a phase shift, and $F(\mathbf{k})$ a given amplitude.

Here, it is approximated by truncating the series to its leading term [23], leading to the implicit relations for the Schwarz's 'P', Schoen's 'G' and Schwarz's 'D' respectively:

$$\cos(X) + \cos(Y) + \cos(Z) = \phi_i, \tag{3}$$

$$\sin(X)\cos(Y) + \sin(Z)\cos(X) + \sin(Y)\cos(Z) = \phi_i, \tag{4}$$

$$\sin(X)\sin(Y)\sin(Z) + \sin(X)\cos(Y)\cos(Z) + \cos(X)\sin(Y)\cos(Z) + \cos(X)\cos(Y)\sin(Z) = \phi_i, \tag{5}$$

where X, Y, and Z are respectively equal to $\Lambda_i 2\pi x_i/L_{ref}$, ϕ is an iso-level controlling the porosity ϕ of the medium, and $L_{ref} = 2$ mm is the unit cell reference length. This unit cell reference length was chosen to obtain a ratio of pore

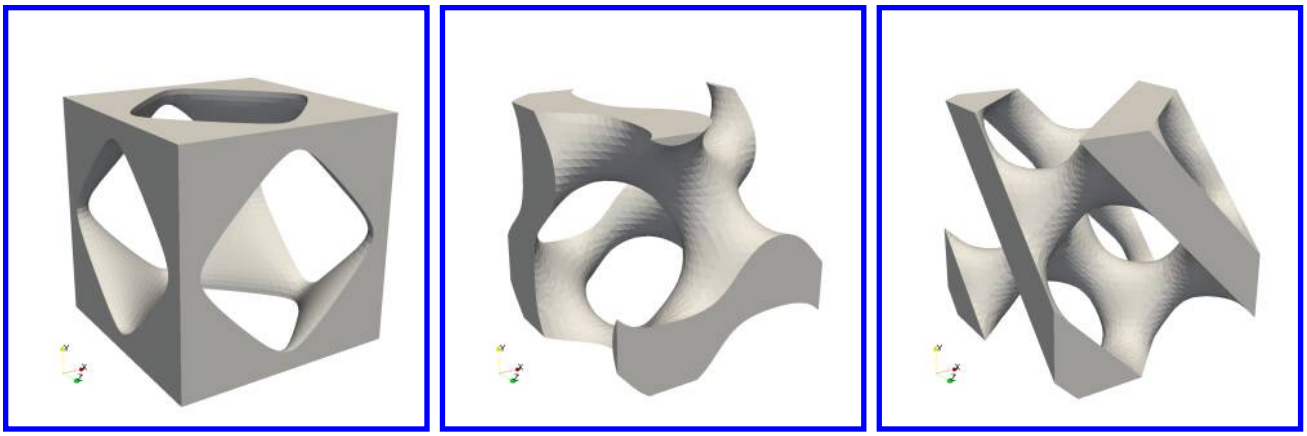

(a) P075 **(b) G075** **(c) D075**

Fig. 2 Unit cells

Table 1 Geometric generation parameters of the TPMS unit cells considered.

Case	L_{ref} [mm]	Λ	θ
P075	2	(1, 1, 1)	$\pi/2$
G075	2	(1, 1, 1)	$acot\left(\frac{EllipticK[1/4]}{EllipticK[3/4]}\right)$
D075	2	(1, 1, 1)	0

diameter to boundary layer thickness $d_p/\delta \approx 17\%$. This ratio, as well as the porosity of 75%, was chosen as it is in the range of parameters which have been observed to lead to the largest noise reduction potential in Ref. [24]. The corresponding unit cells for the Schwartz' 'P' ('Primitive'), Schoen's 'G' ('Gyroid'), and Schwartz' 'D' ('Diamond') are shown in Figure 2. In this study, the 75% porous Schwarz's 'P', Schoen's 'G' and Schwarz's 'D' are referred to as **P075**, **G075**, and **D075** respectively. The descriptions of the porous media of interest enable the creation of a complex design space described by the parameters: θ, Λ_i, ϕ, and L_{ref}.

The discrete geometries were obtained by generating triangulated iso-surfaces in MATLAB and input in 3DS PowerFLOW to fully resolve the porous medium. PowerFLOW is a CFD solver based on the Lattice Boltzmann Method, solving the wall modelled VLES flow field. The geometry uses a resolution of 32^3 nodes in each direction. This was determined to be sufficient since the local geometrical curvature is well approximated [22].

The simulations are further divided into three principal test cases: the smooth walled case (**S**), the communicating case with the same flow conditions in both channels (**C**), and the communicating case with the different flow conditions in both channels (**D**). Case **D** has approximately twice the forcing acting on the bottom channel, while the forcing in the top channel remains unchanged compared to case **C**. This results in a variation of the bulk velocity and in turn the drag of the porous medium. The difference in velocities between the channels is used as an analogy for the lifting conditions for a porous trailing edge, since the pressure gradient between the two boundary layers is not necessarily significant. The following nomenclature is therefore used to refer to the different cases: first the letter to indicate the test case (**S/C/D**), followed by the geometry (**P075/G075/D075**). For example, **D-G075** refers to the pressure differential case with the Schoen's 'G' porous medium. The relevant non-dimensionalisation and Reynolds numbers are used to perform the comparison of interest between non- and lifting conditions.

A. Material properties

The chosen approach to generate the porous media of interest in this study requires additional characterisation in order to map the current design space to the existing literature, which primarily focuses on material properties instead of geometrical properties.The latter geometrical properties allow for the consistent generation of porous media whose material properties can still be obtained.

For porous media, the material properties are determined assuming that the material presented in the preceding subsection can be modelled using the Forchheimer corrected Darcy law, as shown in Equation 6. Where, in this equation,

Table 2 Pressure drop simulation parameters and results. The quadratic fit is of the form $a_1 v_D + a_2 v_D^2 = \Delta p/t$.

Geometry	Δy [m]	a_1	a_2	r^2	K $[m^2]$	C $[1/m]$
P075	6.25×10^{-5}	1107	455	1	3.93×10^{-8}	904
G075	4.16×10^{-5}	1050	644	1	2.78×10^{-8}	857
D075	6.25×10^{-5}	1681	889	1	2.01×10^{-8}	1372

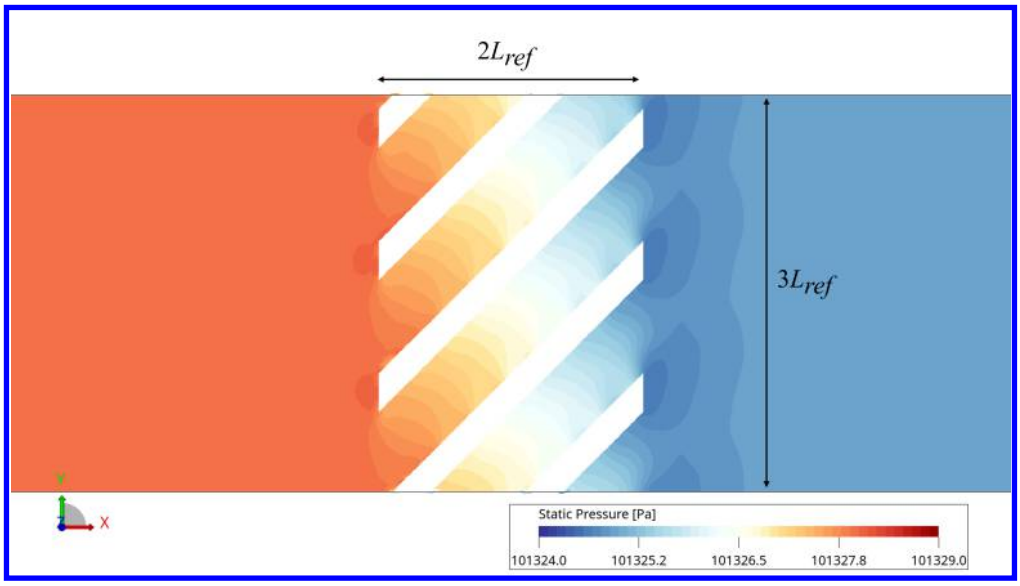

Fig. 3 Near pressure field at $v_D = 0.25$ m/s for D075 at z=0mm.

Δp is the pressure differential across the porous medium, t is the material thickness, μ is the fluid dynamic viscosity, ρ the fluid density, v_D the Darcy velocity, K_i is the permeability along the i-the component and C_i the inertial permeability, also referred to as the form coefficient. Note that the reciprocal of the permeability is also used in literature, referred to as resistivity r.

$$\frac{\Delta p}{t} = \frac{\mu}{K_i} v_D + \rho C_i v_D^2 \tag{6}$$

Thin porous media differ in their behaviour to thick porous media ($t > 50 d_p$) as the material properties show a dependency on the thickness. The porous media are expected to behave like thin porous media following the observations in both material science [25] and previous work on porous trailing edges [9, 10]. It was therefore chosen to characterise the porous media in this study using the thickness $t = 2L_{ref}$.

The pressure drop was measured numerically in a similar numerical setup as the channel flow simulations by computing the difference in pressure 50 mm from the porous media, as shown in Figure 3. The domain size used is $(50mm + t + 50mm) \times 3L_{ref} \times 3L_{ref}$. This was done as there is evidence that measuring the pressure in the vicinity of the porous medium, as was done in [26], would underestimate the pressure drop significantly for thin porous media, with inertial effects playing a large role in the pressure recovery and total pressure drop. This is further confirmed by the observation of the pressure field in Figure 3. The pressure drop would be underestimated by over 10% for this particular case, and this value would be larger for higher Darcy velocities. This discrepancy appears small but compounds to give erroneous measurements of permeability and non-linear permeability.

Both linear and non-linear permeability are then computed by performing a quadratic fit through the obtained points of pressure drop. The resulting measured permeabilities and inertial permeabilities, as well as the simulation and fitting parameters, are summarised in Table 2.

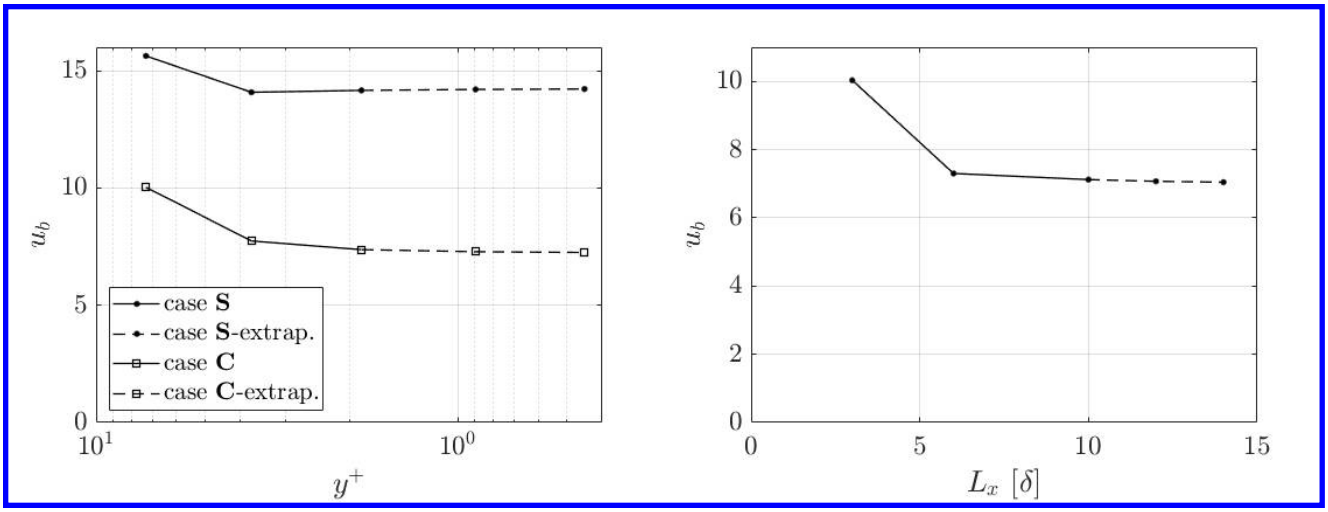

Fig. 4 Grid convergence of bulk velocity versus viscous-scaled wall spacing, smooth wall S and porous C. Dashed lines are the Richardson's extrapolated values.

Fig. 5 Domain convergence of bulk velocity versus streamwise domain length. Dashed lines are the Richardson's extrapolated values.

Table 3 Grid convergence simulation parameters.

Case	Δy [m]	Forcing $\times 10^{-3}$ [N]	Re_b [-]	Re_τ [-]	$N_{\text{voxels}} \times 10^6$ [-]
S-C	2.5×10^{-4}	2.184	10700	590	17.7
S-M	1.25×10^{-4}	2.184	9641	590	17.7
S-F	6.25×10^{-5}	2.184	9696	590	17.7
C-**P075**-C	2.5×10^{-4}	2.184	6895	702	44.2
C-**P075**-M	1.25×10^{-4}	2.184	5299	737	44.2
C-**P075**-F	6.25×10^{-5}	2.184	4998	759	44.2

B. Grid convergence

Grid independence is achieved by capturing both the flow features accurately, as well as the geometry of the porous medium. The grid convergence was performed by computing the bulk velocity u_b as a function of the viscous-scaled wall resolution. The viscous-scaled wall resolution is defined as $y^+ = y/\delta_\nu = y/Re_\tau$, with y the first voxel from the surface, and the bulk velocity is defined as the mean velocity in the channels (i.e. excluding the porous medium).

The parameters of the grid convergence simulations can be seen in Table 3, for all coarse (C), medium (M) and fine (F) resolutions. These are defined as having 8, 16 and 32 voxels/L_{ref} respectively. In this analysis both the **S** and **C** cases use the friction velocity $u_\tau = \sqrt{\tau_w/\rho}$ of case **S** to compute y^+. The asymptotic value was obtained by Richardson extrapolation for resolutions $y^+ \leq 1$.

The results of the grid convergence can be observed in Figure 4. In this figure, one can observe that, while a grid spacing of $y^+ < 3$ appears to be sufficient for the **S** case, a resolution of $y^+ \approx 3$ leads to a large discrepancy in the prediction of drag for the porous medium case **C**. This discrepancy in simulation accuracy can be attributed to the complex geometry that needs to be resolved, as shown in Figure 1. For low resolutions, the geometry is under-resolved, as too few voxels can be used to capture the continuous variations in wall geometry. Therefore, a grid spacing of 32 voxels/L_{ref} was chosen for the rest of the analysis. Note, due to the thin parts of the geometry for **G075**, a resolution of 48 voxels/L_{ref} was necessary to ensure a watertight simulation (the refinement of the grid requiring a multiple of 16 to be used).

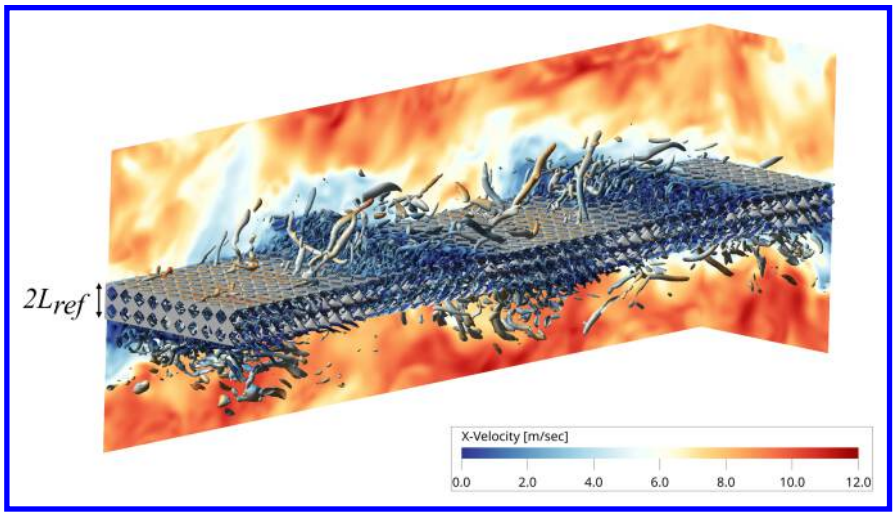

Fig. 6 Instantaneous solution of case C-LD ($L_x \times L_y \times L_z = 10\delta \times (t + 4\delta) \times 2\delta$), with iso-surfaces of constant $\lambda_2 = -1 \times 10^{-7}$ coloured by streamwise velocity. The first cell of P075 is cut to show the internal flow topology.

Table 4 Domain sizing simulation parameters.

Case	$L_x \times L_y \times Lz$ [m]	Δy [m]	$\overline{y^+}$ [-]	Forcing $\times 10^{-3}$ [N]	$N_{\text{voxels}} \times 10^6$ [-]
C-P075-SD	$3\delta \times (4\delta + t) \times 1.6\delta$	6.25×10^{-5}	0.89	0.874	17.4
C-P075-MD	$6\delta \times (4\delta + t) \times 2\delta$	6.25×10^{-5}	0.97	2.184	44.2
C-P075-LD	$10\delta \times (4\delta + t) \times 2\delta$	6.25×10^{-5}	1.07	3.638	72.4

C. Domain sizing

An analysis of the impact of the domain dimension was performed due to the previously documented durable spanwise coherent turbulent structures convected in the periodic domain [27]. These spanwise coherent turbulent structured can be seen in Figure 6. These are assimilated to wall transpiration as they force a wall normal velocity component at the boundary of the porous medium, as shown by the colouring of the iso-surfaces of λ_2 criterion.

It has been documented in Ref. [28] and [29] that the presence of wall transpiration in turbulent channel flows can both reduce and increase drag significantly for smooth walls. Therefore, this analysis seeks to quantify the impact of these turbulent structures on the bulk velocity, which is in turn related to the drag imparted by the porous medium.

The dimensions of the domain were obtained by comparing the dimension and convection velocity of the spanwise coherent turbulent structures for domains of dimensions $L_x \times L_y \times L_z$, where $L_y = t + 4\delta$ remains fixed. The first has dimensions corresponding to the best practices for rough walls referred to as the Small Domain (SD) ($3\delta \times L_y \times 1.6\delta$) [19], where the spanwise extent was increased to allow for an integer number of porous cells. The second of dimension ($6\delta \times L_y \times 2\delta$) corresponds to the smallest recommended domain dimension for TCF over smooth walls, referred to as Medium Domain (MD) [30]. Finally, the last domain, of dimension ($10\delta \times L_y \times 2\delta$), corresponds to the maximum streamwise dimension of the porous extent in practice [12], referred to as Large Domain (LD). The simulation parameters are summarised in Table 4.

The domain sizing study results are shown in Table 5 for the case **C-P075**. Figure 5 shows that the mean velocity in the channels, u_b, does converge with an increase in the domain size. Therefore, the adopted streamwise length L_x was

Table 5 Domain sizing simulation results.

Case	Re_b [-]	Re_τ [-]	Re_{conv} [-]	$L_{coh.}/\delta$ [-]
C-P075-SD	6888	697	4299	1.2
C-P075-MD	4998	753	4299	2.1
C-P075-LD	4879	750	4308	2.0

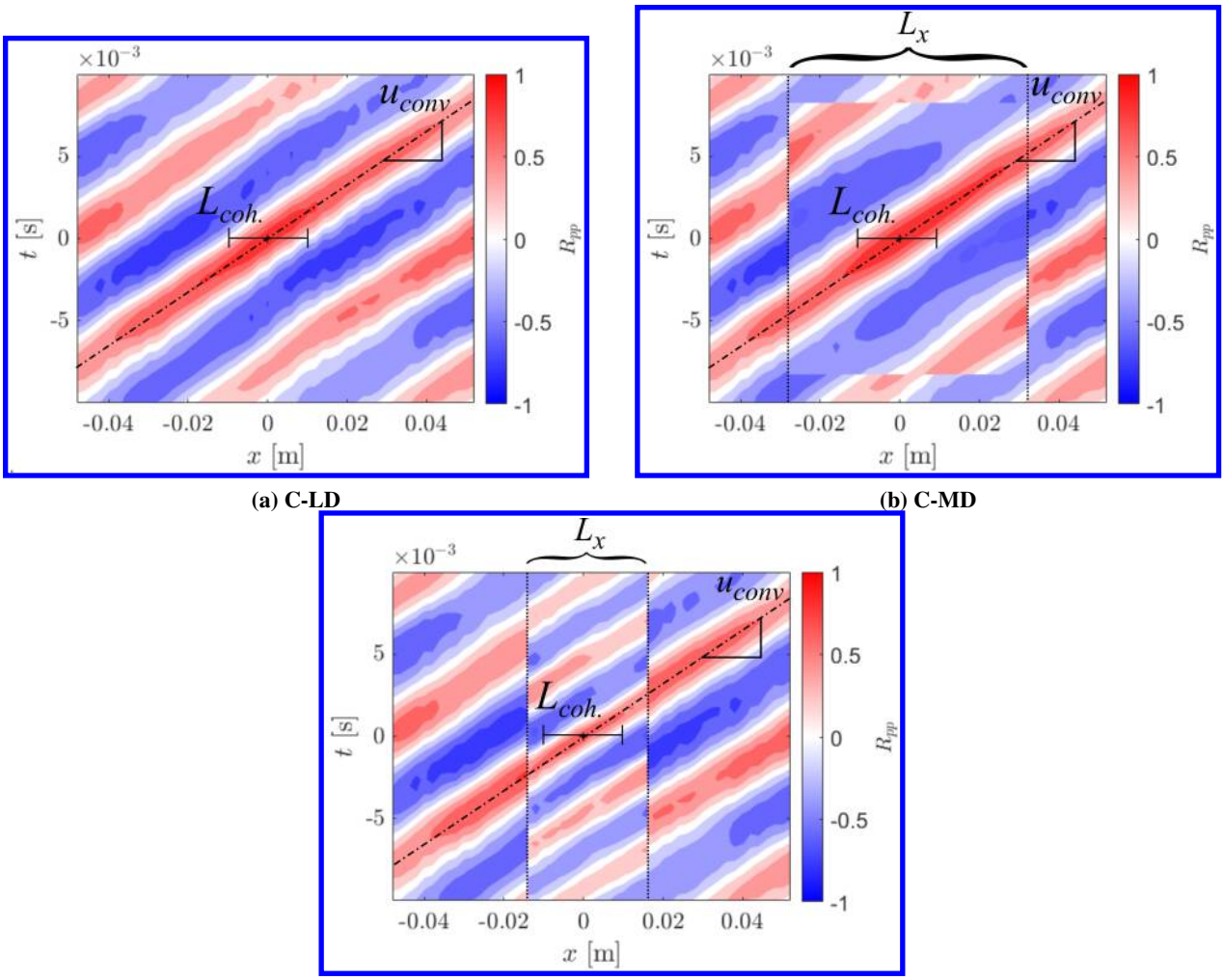

(a) C-LD **(b) C-MD**

(c) C-SD

Fig. 7 Spatio-temporal correlation of the pressure signal in the centre of the top channel at $y = 0.1$mm ($y^+ \approx 100$), for the porous medium P075.

chosen to be equal to 6δ on grounds of computational cost and accuracy.

The source of the drag error as a function of the domain size can be explained by the presence of the aforementioned spanwise coherent turbulent structures. The characteristics of these structures can be quantified by computing the spatio-temporal correlation of the pressure signal with respect to a point in the centre of the domain at a distance $y = 0.1$ mm from the porous medium ($y^+ \approx 100$). The results are shown in Figure 7, where each case is overlaid over the largest case **C**-LD. In this figure, the alternating correlated and anti-correlated bands indicate these structures being convected, the horizontal width of the band corresponds to their dimension, and the inverse of the gradient of these bands is the convection velocity u_{conv}.

For all cases, the convection velocity is accurately captured. However, the dimension of the spanwise structures appears to be dependent on the domain size for small domains. This can be partly explained by the previously cited work on walls with transpiration [29]. Both the velocity and wavelength of the transpiration influences the drag alteration. In the case of interest, the convection velocity corresponds to a region of large drag increase in Ref. [29].

Table 6 Summarising table of the test cases. Numbers in brackets indicate the top and bottom channels respectively.

Case	Δy [m]	Forcing $\times 10^{-3}$ [N]	Re_b [-]	Re_τ [-]	Re_{conv} [-]	$N_{\text{voxels}} \times 10^6$ [-]
S	6.25×10^{-5}	2.184	9696	590	8213	17.7
C-P075	6.25×10^{-5}	2.184	4998	753	4101	44.2
D-P075	6.25×10^{-5}	(2.184, 4.532)	(6435, 9790)	(712, 1088)	(4805, 6712)	44.2
C-G075	4.16×10^{-5}	2.184	3626	770	3781	66.4
D-G075	4.16×10^{-5}	(2.184, 4.532)	(5118, 5243)	(735, 1109)	(5108, 5293)	66.4
C-D075	6.25×10^{-5}	2.184	3973	760	3834	44.2
D-D075	6.25×10^{-5}	(2.184, 4.532)	(5244, 5458)	(731, 1098)	(5097, 5472)	44.2

Table 7 Summarising table of the drag decomposition for the test cases. Numbers in brackets indicate the top and bottom channels respectively.

Case	Δu^+ [-]	l_T^+ [-]	Total Drag $[N/m^2]$	Friction Drag [%]	Pressure Drag [%]	$\Delta Drag$ [%]
S	-	0	0.905	100	0	0
C-P075	13.8	11	0.603	35	65	674
D-P075	(11.2, 14.4)	(16, 14)	0.872	34	66	(358, 652)
C-G075	15.7	27	0.573	21	79	1113
D-G075	(13.6, 15.7)	(29, 21)	0.785	20	80	(725, 981)
C-D075	15.0	25	0.503	20	80	901
D-D075	(13.4, 15.4)	(24, 17)	0.694	19	81	(635, 926)

III. Results

The results are divided into three parts. The first focuses on the drag of the porous medium while the second on the impact on the fluctuating properties. Finally, the third section of the results relates material parameters and the aerodynamic performance. For both cases **C** and **D**, they are compared relative to the performance of a smooth wall. The characteristics of the simulations are given in Table 6.

A. Aerodynamic performance

The aerodynamic performance of the porous media is quantified using the difference in the viscous scaled velocity profiles [31], defined as the velocity deficit. In Ref. [31], the scope is limited to drag altering surfaces. The method consists in identifying the location of the origin of the near-wall cycle of velocity fluctuations and define the offset to the surface of the porous medium to be the virtual origin, the coordinates are then taken to be $y^+ + l_T^+$. l_T^+ being the turbulence penetration length. This length, defined as the perceived wall position for the outer flow, is determined by shifting the Reynolds shear stress profile to match the region about $y^+ = 10$. The only difference here being that the outer flow is more heavily modified than for roughness [31] or acoustic liners [19].

This method enables the profiles to be defined as a function of their virtual origin, and to subtract the log-layers to obtain the velocity deficit, and as a result the drag increase. The obtained values for the virtual origins are shown in Table 7. They are large with respect to previously documented values [19] indicating that the near wall cycle is greatly modified by the presence of both the porous media and the communication between the two boundary layers.

The viscous scaling based on the friction velocity u_τ is obtained by performing a force balance in the channels and computing the equivalent wall shear stress for a smooth wall to provide equilibrium to such system, using the relation in Equation 7. The obtained friction velocities and Reynolds numbers are provided in Table 6.

$$u_{\tau,eq} = \sqrt{\frac{\text{Forcing} - \int \tau_w}{L_x \times L_z \times \rho}} \tag{7}$$

The obtained viscous-scaled velocity profiles for cases **C** and **D** are presented in Figure 8 and Figure 10 respectively.

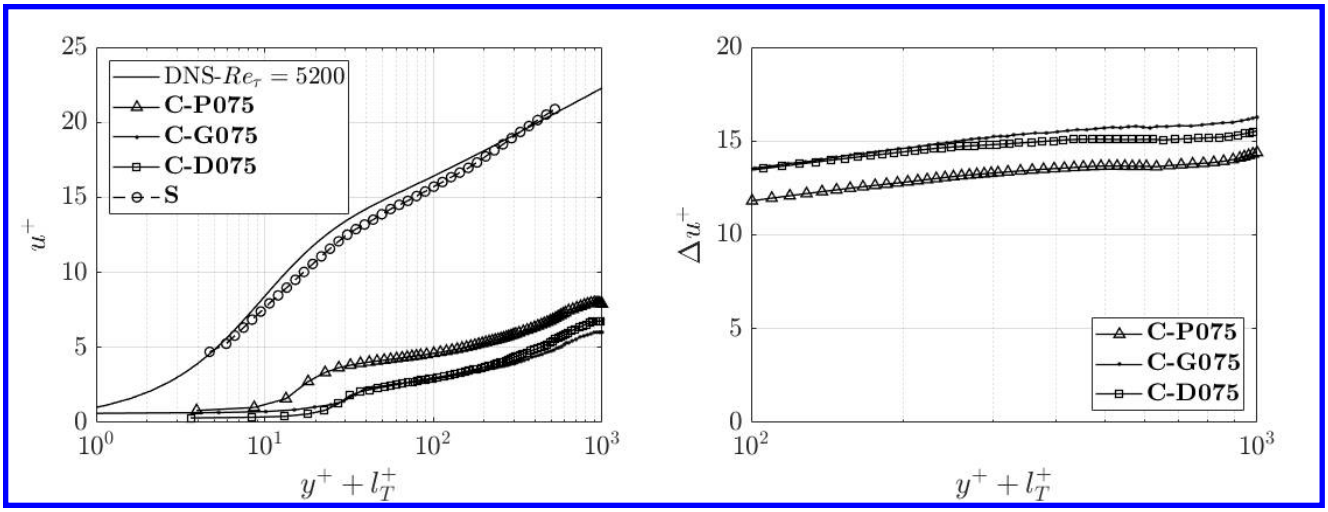

Fig. 8 Viscous-scaled velocity profiles for all porous geometries for case C. DNS results are from Ref. [32].

Fig. 9 Viscous-scaled velocity deficit for all porous geometries for case C.

Alongside these velocity profiles, the velocity deficit is also shown in Figure 9 for cases **C** and Figure 11 for cases **D**. To compute the mean velocity deficit for each case, the mean value of Δu^+ is computed over the interval of the viscous-scaled wall normal coordinate $300 < y^+ < 700$.

In Figure 8, the buffer layers are aligned, as intended by the use of the virtual origin and despite the values of turbulence penetration length being large. Moreover, a slip velocity of $0.3u^+$ to $0.8u^+$ is observed. The slip velocity indicates that a hydrodynamic field is present in the porous medium for all cases, with a mean axial velocity field existing in the porous media. An increase in internal streamwise velocity leads to an increase in drag. In particular, pressure drag increases rapidly due to the work done by the flow to drive this internal flow and generate the required internal pressure gradient to enable the streamwise internal flow. The role of pressure drag is further discussed in the upcoming sections.

Additionally, from Figure 8 and Figure 9, despite the spanwise turbulent structures being convected in the near porous medium region, the log-layer is present. The medium Reynolds numbers chosen in this study are sufficient for the presence of a log-layer at a greater distance from the wall. The additional transitional layer between the buffer layer and the log-layer ($50 < y^+ < 300$) appears to be mainly driven by the spanwise coherent turbulent structures previously mentioned.

Finally, both the **G075** and **D075** porous geometries appear to behave similarly, with **G075** performing slightly worse. This points to the existence of a topological difference between these two geometries and **P075** that would result in a lower drag increase for the latter.

For cases **D**, as shown in figures 10 and 11, the story is similar for the most part. Nonetheless, the drag increase is more significant on the higher velocity boundary layer, which would be the suction side of an airfoil. The difference in aerodynamic performance between the two communicating boundary layers is greater for the **P075** porous geometry. This further confirms that this latter geometry behaves differently to the other two. This is also seen in Table 6, where the convection velocity of the near-wall turbulence and the bulk velocity is similar for both **G075** and **D075** geometries, whereas they communicate less for **P075**. This is counter-intuitive since the latter geometry has the largest permeability and it would be expected that this would lead to greater communication between the two grazing flows. The communication is here defined as the correlation between the pressure signals on both sides of the porous medium.

An indication for the reason for **P075** to behave differently is present in Table 7. In this table, the turbulence penetration length l_T^+ is smaller for **P075** than the other geometries. The penetration length, being the flow perceived location of the wall, is not only related to the drag increase [31] but also is informative of the fluctuations impinging on the porous medium. A large value of l_T^+ indicates a large amount of near-wall and internal fluctuations, which in turn generates both friction and pressure drag.

The drag increase was computed based on the wake drag Equation 8 [33], as documented in Table 6. It can be observed that while the drag increase due to the porous medium is very large, it is different on both sides of the TPMS when different flow conditions are present. This is due to the velocity of the spanwise coherent turbulent structures differing between the cases *C* and *D*. When the flow conditions are the same on both sides of the porous medium, the

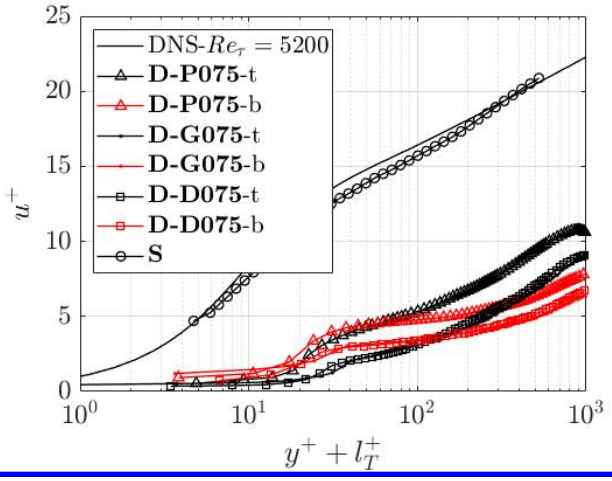

Fig. 10 Viscous-scaled velocity profiles for all geometries for case D. The top boundary layer is in black and the bottom in red. DNS results are from Ref. [32].

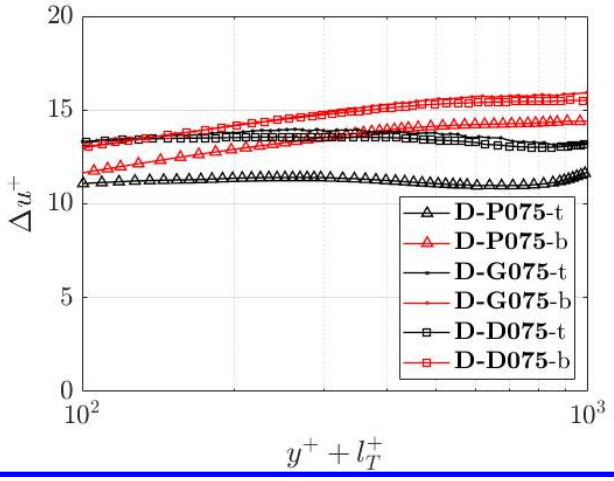

Fig. 11 Viscous-scaled velocity deficit for all geometries for case D. The top boundary layer is in black and the bottom in red.

natural convection velocity of the system can be reached. However, when different flow conditions are present on both sides of the porous medium, this equilibrium is not reached since both boundary layers effectively operate at a different natural frequencies. This result in a convection velocity that is a proportional to the mean velocity of both channels (i.e. $U_{conv} \propto \sum U_{b,i}$).

$$\Delta\text{Drag}(\%) = \frac{1}{(1 - \Delta u^+/u_c^+)^2} - 1 \tag{8}$$

The relationship between the convection velocity of the spanwise coherent turbulent structures and the spatio-temporal correlation is further analysed in Figure 12. In each sub-figure, the spatio-temporal correlation of the pressure signal is shown for the top and bottom channels of case **D-P075** and the bottom channel of case **C**. For case **D-P075**-bottom and case **C-P075**, clear correlated signals can be observed indicating structures being convected. In contrast, Figure 12b shows a break-down of these structures in the slower of the two channels (i.e. the pressure side). This agrees with the drag being lower as less low velocity fluid is injected in the top channel. Moreover, the gradient is shallower. In this context, it results in a lower drag in the top channel of case *D* since the coherent structures are faster, and thus provide less drag than in case *C*.

It can be concluded that preventing the onset of these spanwise coherent turbulent structures will reduce the aerodynamic penalty of a porous trailing edge. The drag increase remains to be quantified and can be done as per Equation 8. The values are summarised in Table 7. The drag increase with respect to the smooth wall case is considerable and presents a 3.5 to over 11 times increase.

It is also important to note that the drag can be decomposed in its two components present here, being the force acting tangential to the surface of the porous media and normal to it. The former is the result of friction drag and the latter of pressure drag. For each geometry, this was computed and the decomposition is largely independent of the flow conditions and topology. This points to the ability to tailor a porous medium for aerodynamic performance since its drag decomposition is easily predicted.

B. Wall pressure spectrum

The wall pressure spectrum of the TPMS Schwarz's P porous medium was computed to explore the impact of the observed convected turbulent structures and the communication between the boundary layers on the fluctuating properties at the surface of the material. The wall pressure spectra is related to the acoustic signature as the pressure fluctuations impinging on the surface are scattered and convected to the far-field [34]. It must be noted that higher frequencies are less efficiently scattered to the far field, as observed in Ref. [12].

The wall pressure spectra are given in Figure 13, in dB for a reference value of 1 Pa. In this figure, it is possible to observe that the power spectral density is lower for case **C** than for case **S** across frequencies smaller than 600Hz. This

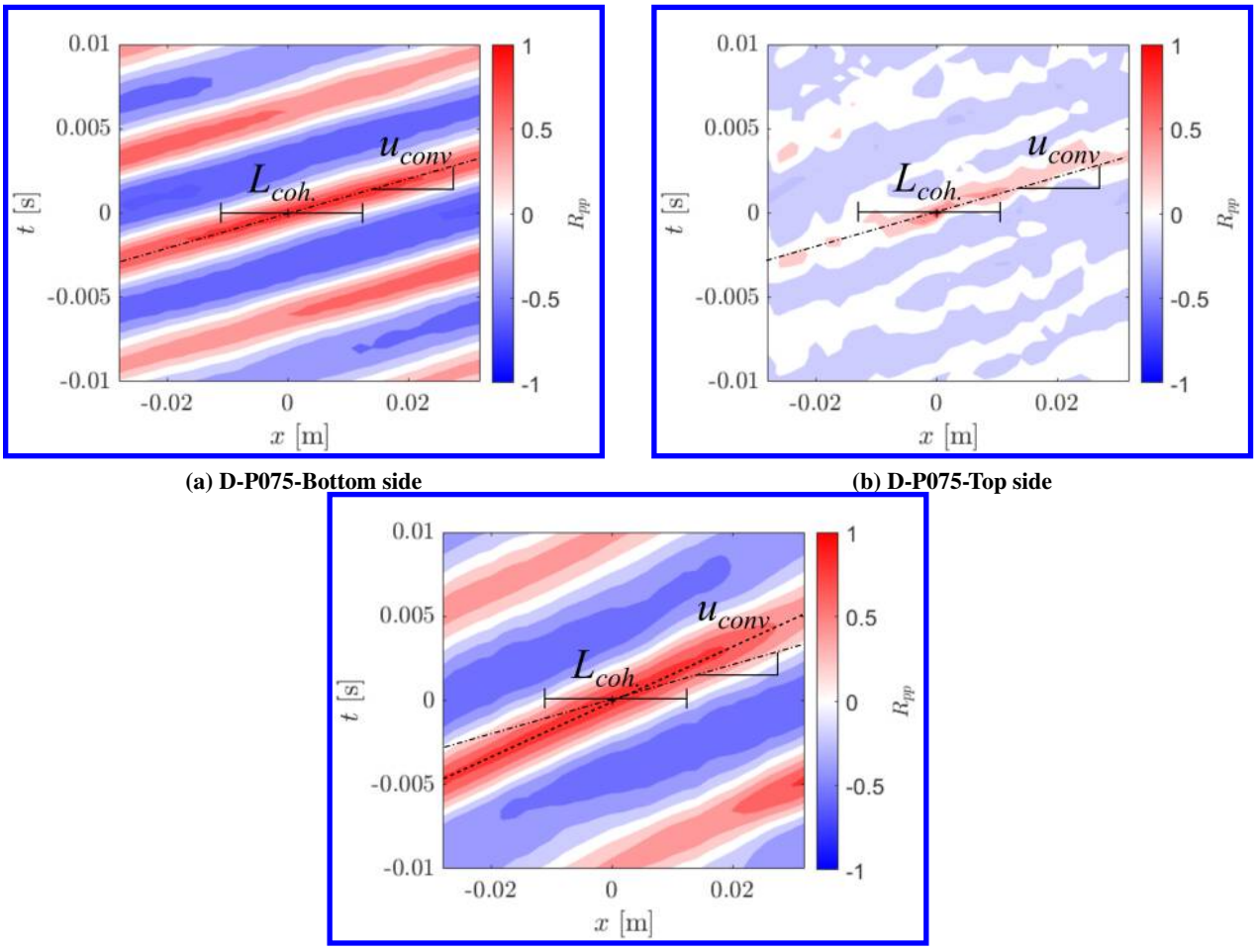

(a) D-P075-Bottom side

(b) D-P075-Top side

(c) C-P075

Fig. 12 Spatio-temporal correlation of the pressure signal in the centre of the channels at $y = 0.1$mm ($y^+ \approx 100$).

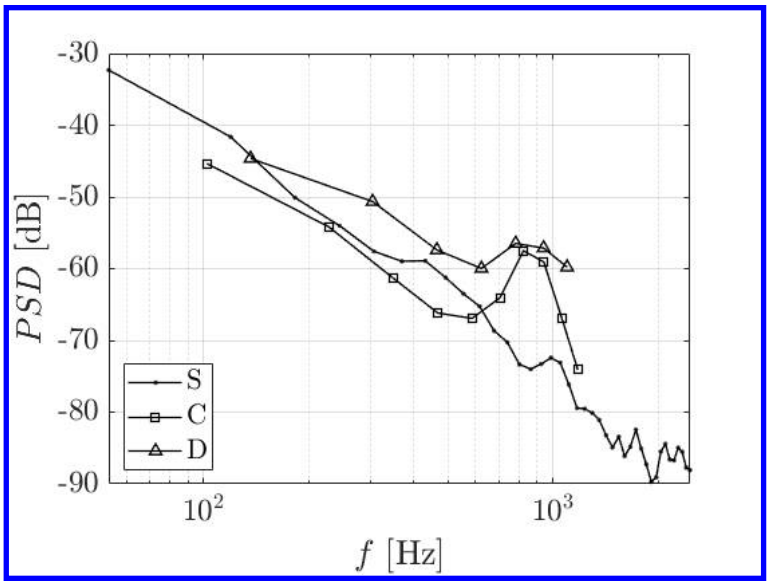

Fig. 13 Wall pressure spectra of the power spectral density as a function of frequency, normalised with respect to 1 Pa for the P075 porous geometry.

corresponds to the range of frequencies where noise reduction is observed [34]. This is not observed in case **D** when the velocity on both sides of the porous medium is different.

The analysis of the wall pressure spectrum also points towards the onset of a tonal noise due to the presence of a peak at 850 Hz for both cases **C** and **D**. This is consistent with the observations of tonal noise for porous trailing edges in Ref. [11]. This asymptotic regime for porous trailing edges should be avoided but appears to be present at low Reynolds numbers for certain geometries of airfoil [35]. The increase in energy present in the large frequencies also tends towards previous observations, such as Ref. [6]. This is partly explained by the enhanced mixing present in the boundary layers, induced in part by the topology of the porous medium and the spanwise coherent turbulent structures injecting low velocity fluid in the boundary layer and forcing high velocity fluid in the porous medium.

The present analysis points to the ability to maximise communication between two communicating grazing flows by designing the porous trailing edge to have similar flow conditions on both sides. While this will benefit the pressure release mechanism, it will also lead to the onset of spanwise coherent turbulent structures, greatly increasing drag.

C. Aerodynamic performance and material characterisation

This section focuses on relating the previously presented results to the material and geometric properties. The state-of-the-art was primarily interested in relating the material properties to the aeroacoustic performance of porous media and porous trailing edges. The drag increase is therefore plotted with respect to the inverse of the non-linear permeability $1/C^+$ and $\sqrt{K^+}$.

From these figures, it is apparent that the relationship between conventional criteria based on the material properties are no longer sufficient to explain the drag increase of communicating flows about porous media. The discrepancy can be explained by the differences in both flow and geometric topology.

In the case of grazing flows over rough or porous media, the outer flow is unchanged with respect to a smooth wall and the modification of the flow topology is mainly limited to the inner and buffer layer [19]. The present study was able to show that the flow topology is different with the communication between the channels, resulting in different velocity profiles.

Figure 16 shows the mean streamwise velocity for case **C-P075**. As can be seen in the figure, the porous geometry and its streamwise component allows for the flow to not only penetrate the medium but also interact with the internal geometry. The low velocity regions downstream of the geometrical features is associated to a lower pressure, thus increasing the pressure drag.

Similarly, the fluctuating velocity field shown in Figure 17 shows regions of large velocity fluctuations interacting with the geometrical features. The magnitude of these fluctuations are comparable or larger in magnitude than the

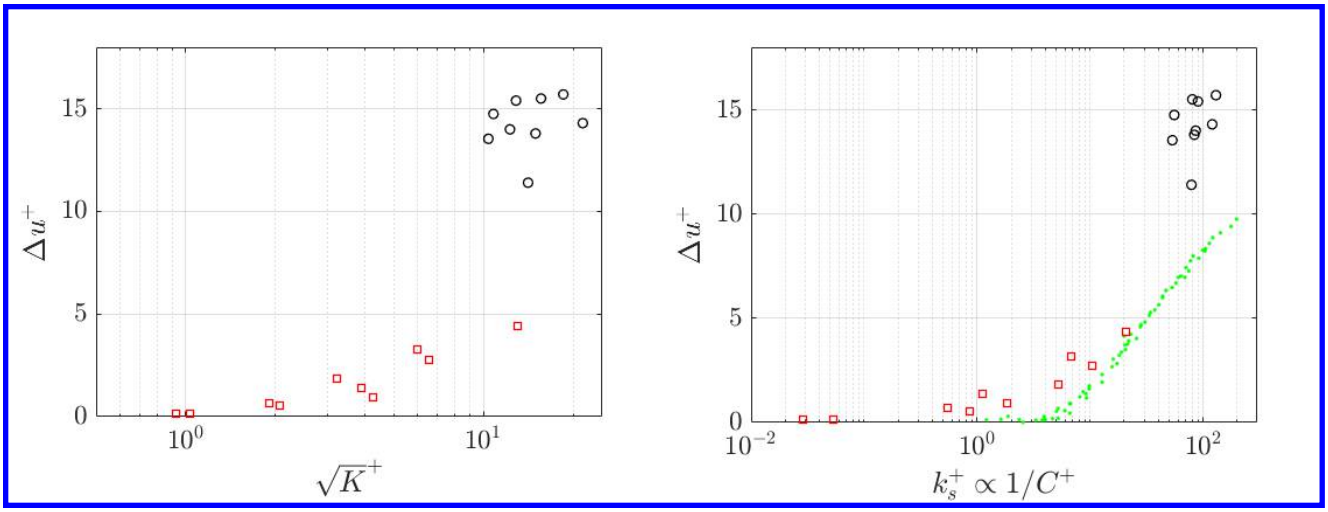

Fig. 14 K vs Δu^+. In red squares, data from Ref. [19] and black circles this study.

Fig. 15 C vs Δu^+. In red squares, data from ref. [19], green dots from Ref. [36] and black circles this study.

mean field. This indicates that although there is no mean flow through the porous medium, the instantaneous pressure differential across the porous medium is large enough to allow for the shedding and instantaneous flow through.

Finally, the porous medium behaves differently in wall-normal and streamwise direction. As mentioned in the section on the material properties of porous media, for thin porous media, the material properties are dependent on thickness [25]. However, in the streamwise direction, the porous medium can be considered to be thick. This implies that the permeability cannot be solely considered to be a sector but a matrix, further hindering our ability to model the observed behaviour. It can therefore be concluded that the geometry itself has a much stronger correlation with the increase in drag. In particular, the dimensions relating to the porous surface in streamwise and wall-normal directions should be considered since they are related to the internal hydrodynamic field and the flow penetration in the porous medium respectively.

IV. Conclusion

In conclusion, this study presented a novel numerical setup aimed at characterising the interaction between turbulent boundary layers through a porous medium. This was justified in order to further our understanding of the porous trailing edge noise reduction, and the observed aerodynamic penalty. The setup is constructed by vertically stacking two temporally developing turbulent channel flows and allowing them to communicate through a fully resolved porous medium. The porous media of interest in this study are based on the 75% triply periodic minimum surfaces of type P, G and D. Specifically, two cases are compared. The first is an analogy for the zero-lift conditions, in which the noise reduction potential of porous media is greatest. The second is an analogy for lifting conditions, where the noise reduction potential is known to decrease. The different conditions were obtained by varying the forcing in the channels independently.

The aerodynamic performance of the porous medium was first established. It was observed that the different flow conditions impact significantly the porous media performance. The drag was quantified by computing the viscous-scaled velocity deficit. The drag was found to greatly increase in the presence of porous media, increasing between 3.5 and 11 times with respect to the drag of a smooth wall. This was related to the presence of spanwise coherent structures, which both facilitate the communication between the two boundary layers and favour high velocity flow interacting with the geometry. The drag increase is therefore driven by the mixing of the low velocity hydrodynamic field present in the porous medium and the grazing boundary layers.

The principal difference between cases **C** and **D**, representing the zero-lift and lifting conditions, was limited to the convection velocity of the spanwise coherent turbulent structures. They are slower in the zero lift conditions and introduce a significant increase in drag. In the differential case, the convection velocity is larger but not directly proportional to the velocity of the channel but that of the system (i.e. of the combined velocities on both sides of the porous medium). Moreover, the velocity deficit is reduced in the vicinity of the porous medium since the structures are

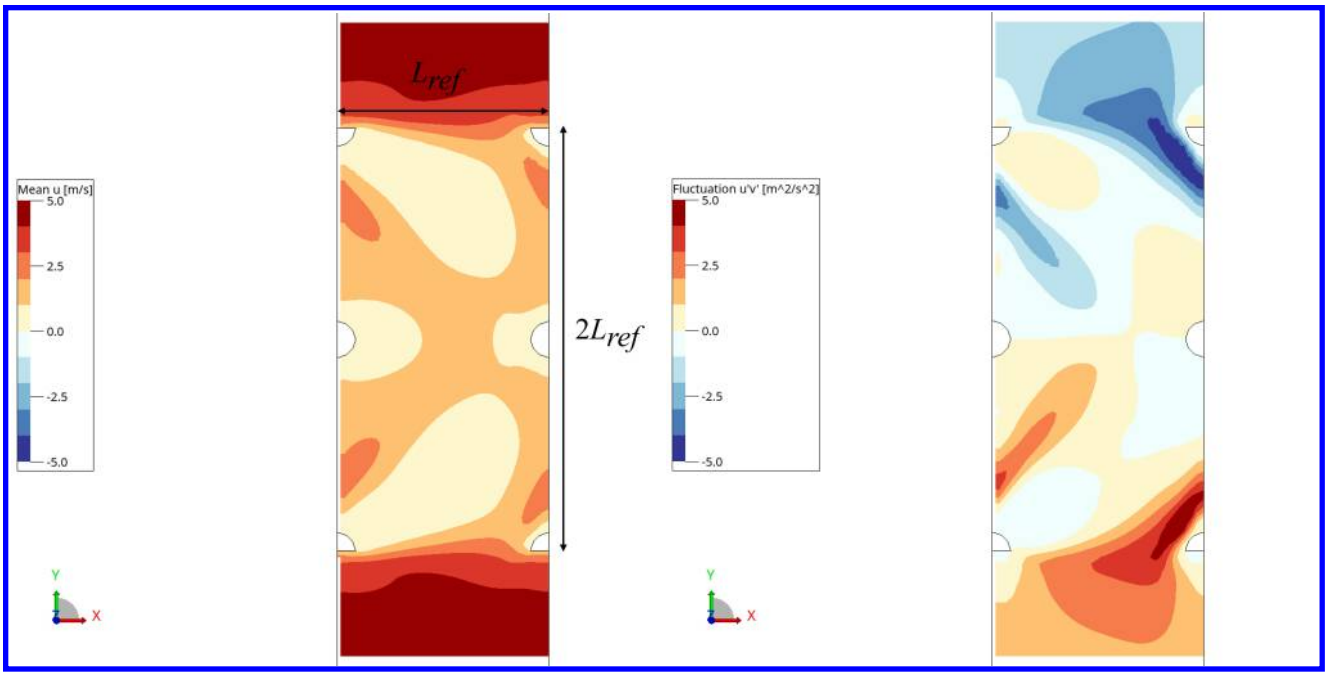

Fig. 16 Mean streamwise velocity in a unit cell of P075.

Fig. 17 Reynolds shear stress in a unit cell of P075.

weaker.

The surface pressure spectra on the porous medium surface was also computed. A reduction of the power spectral density at the range of frequencies where noise reduction occurs was observed. As this was less efficient at lifting conditions, a decrease in noise reduction potential would be expected. The shift in peak surface pressure spectra between zero-lift and lifting conditions was related to the convective velocity of the spanwise coherent turbulent structures. This velocity was found to be solely a function of the velocities on both sides of the porous medium.

Should the onset of the strong spanwise coherent turbulent structures be delayed or avoided, it can be hypothesised that the drag and lift penalties can be largely reduced, being dominated by non-linear friction. This is still compatible with the promotion of the pressure release mechanism, being dominated by linear permeability and unsteady effects. The decorrelation of aerodynamic and acoustic performance points to the potential of tailoring porous media for a wider range of operating conditions.

Finally, it was observed that the present study does not fall in the canonical relationships between drag increase and material properties for grazing flows over rough surfaces. This was attributed to geometrical and flow topology differences between the present study and the literature.

References

[1] Jones, L. E., and Sandberg, R. D., "Acoustic and hydrodynamic analysis of the flow around an aerofoil with trailing-edge serrations," *Journal of Fluid Mechanics*, Vol. 706, 2012, pp. 295–322. https://doi.org/10.1017/jfm.2012.254.

[2] Avallone, F., van der Velden, W. C. P., Ragni, D., and Casalino, D., "Noise reduction mechanisms of sawtooth and combed-sawtooth trailing-edge serrations," *Journal of Fluid Mechanics*, Vol. 848, 2018, pp. 560–591. https://doi.org/10.1017/jfm.2018.377.

[3] Arce León, C., Ragni, D., Pröbsting, S., Scarano, F., and Madsen, J., "Flow topology and acoustic emissions of trailing edge serrations at incidence," *Experiments in Fluids*, Vol. 57, No. 5, 2016, pp. 1–17. https://doi.org/10.1007/s00348-016-2181-1.

[4] Geyer, T. F., and Sarradj, E., "Trailing edge noise of partially porous airfoils," *20th AIAA/CEAS Aeroacoustics Conference*, , No. June, 2014, pp. 1–18. https://doi.org/10.2514/6.2014-3039.

[5] Herr, M., Rossignol, K. S., Delfs, J. W., Mößner, M., and Lippitz, N., "Specification of porous materials for low-noise trailing-edge applications," *20th AIAA/CEAS Aeroacoustics Conference*, , No. June, 2014, pp. 1–19. https://doi.org/10.2514/6.2014-3041.

[6] Teruna, C., Avallone, F., Ragni, D., and Casalino, D., "On the noise reduction of a porous trailing edge applied to an airfoil at lifting condition," *Physics of Fluids*, Vol. 33, No. 5, 2021, p. 1ENG. https://doi.org/10.1063/5.0047512.

[7] Ye, Q., Avallone, F., Ragni, D., Choudhari, M., and Casalino, D., "Effect of surface roughness on boundary layer transition and far field noise," *25th AIAA/CEAS Aeroacoustics Conference, 2019*, 2019. https://doi.org/10.2514/6.2019-2551.

[8] Geyer, T., Sarradj, E., and Fritzsche, C., "Porous airfoils: Noise reduction and boundary layer effects," *15th AIAA/CEAS Aeroacoustics Conference (30th AIAA Aeroacoustics Conference)*, Vol. 9, No. 6, 2009, pp. 787–820. https://doi.org/10.2514/6.2009-3392.

[9] Teruna, C., "Aerodynamic Noise Reduction with Porous Materials: Aeroacoustics Investigations and Applications," Ph.D. thesis, Delft Univeristy of Technology, 2022. https://doi.org/10.4233/uuid:260cd874-c1ed-4155-bfdc-cf7fc3813ca6.

[10] Rubio Carpio, A., "Innovative Permeable Materials for Broadband Trailing-Edge Noise Mitigation," Ph.D. thesis, Delft University of Technology, 2021. https://doi.org/10.4233/uuid:fd3d84a7-c162-4cd4-8b19-bee53e00505f.

[11] Luesutthiviboon, S., Ragni, D., Avallone, F., and Snellen, M., "An alternative permeable topology design space for trailing-edge noise attenuation," *International Journal of Aeroacoustics*, Vol. 20, No. 3-4, 2021, pp. 221–253. https://doi.org/10.1177/1475472X211003295.

[12] Teruna, C., Avallone, F., Casalino, D., and Ragni, D., "Numerical investigation of leading edge noise reduction on a rod-airfoil configuration using porous materials and serrations," *Journal of Sound and Vibration*, Vol. 494, 2021, pp. 1–25. https://doi.org/10.1016/j.jsv.2020.115880.

[13] Colbrook, M. J., and Ayton, L. J., "Do we need non-linear corrections? On the boundary Forchheimer equation in acoustic scattering," *Journal of Sound and Vibration*, Vol. 495, 2021, p. 115905. https://doi.org/10.1016/j.jsv.2020.115905.

[14] Shahzad, H., Hickel, S., and Modesti, D., "Permeability and Turbulence Over Perforated Plates," *Flow, Turbulence and Combustion*, Vol. 109, No. 4, 2022, pp. 1241–1254. https://doi.org/10.1007/s10494-022-00337-7.

[15] Rosti, M. E., Brandt, L., and Pinelli, A., "Turbulent channel flow over an anisotropic porous wall – drag increase and reduction," *Journal of Fluid Mechanics*, Vol. 842, 2018, pp. 381–394. https://doi.org/10.1017/jfm.2018.152.

[16] Suga, K., Okazaki, Y., Ho, U., and Kuwata, Y., "Anisotropic wall permeability effects on turbulent channel flows," *Journal of Fluid Mechanics*, Vol. 855, 2018, pp. 983–1016. https://doi.org/10.1017/jfm.2018.666.

[17] Breugem, W. P., Boersma, B. J., and Uittenbogaard, R. E., "The influence of wall permeability on turbulent channel flow," *Journal of Fluid Mechanics*, Vol. 562, 2006, p. 35. https://doi.org/10.1017/S0022112006000887.

[18] Shahzad, H., Hickel, S., and Modesti, D., "Permeability and turbulence over perforated plates," *arXiv*, 2022. http://arxiv.org/abs/2203.04753.

[19] Shahzad, H., Hickel, S., and Modesti, D., "Turbulence and added drag over acoustic liners," *Journal of Fluid Mechanics*, Vol. 965, 2023, p. A10. https://doi.org/10.1017/jfm.2023.397.

[20] Meeks III, W. H., "The Theory of Triply Periodic Minimal Surfaces," *Indiana University Mathematics Journal*, Vol. 39, No. 3, 1990, pp. 877–936.

[21] Gandy, P. J., and Klinowski, J., "Exact computation of the triply periodic Schwarz P ('Primitive') minimal surface," *Chemical Physics Letters*, Vol. 321, No. 5-6, 2000, pp. 363–371. https://doi.org/10.1016/S0009-2614(00)00373-0.

[22] Gandy, P. J., Bardhan, S., Mackay, A. L., and Klinowski, J., "Nodal surface approximations to the P, G, D and I-WP triply periodic minimal surfaces," *Chemical Physics Letters*, Vol. 336, No. 3-4, 2001, pp. 187–195. https://doi.org/10.1016/S0009-2614(00)01418-4.

[23] von Schnering, H. G., and Nesper, R., "Nodal surfaces of Fourier series: Fundamental invariants of structured matter," *Zeitschrift für Physik B Condensed Matter*, Vol. 83, No. 3, 1991, pp. 407–412. https://doi.org/10.1007/BF01313411.

[24] Rubio Carpio, A., Merino Martínez, R., Avallone, F., Ragni, D., Snellen, M., and van der Zwaag, S., "Experimental characterization of the turbulent boundary layer over a porous trailing edge for noise abatement," *Journal of Sound and Vibration*, Vol. 443, 2019, pp. 537–558. https://doi.org/10.1016/j.jsv.2018.12.010.

[25] Baril, E., Mostafid, A., Lefebvre, L. P., and Medraj, M., "Experimental demonstration of entrance/exit effects on the permeability measurements of porous materials," *Advanced Engineering Materials*, Vol. 10, No. 9, 2008, pp. 889–894. https://doi.org/10.1002/adem.200800142.

[26] Asbai-Ghoudan, R., Ruiz de Galarreta, S., and Rodriguez-Florez, N., "Analytical model for the prediction of permeability of triply periodic minimal surfaces," *Journal of the Mechanical Behavior of Biomedical Materials*, Vol. 124, 2021, p. 104804. https://doi.org/10.1016/j.jmbbm.2021.104804.

[27] Hunter, T. P., Doan, N. A. K., Avallone, F., and Ragni, D., "Numerical investigation of communicating turbulent boundary layers through porous media," *INTER-NOISE and NOISE-CON Congress and Conference Proceedings*, Vol. 268, No. 8, 2023, pp. 834–840. https://doi.org/10.3397/IN_2023_0133.

[28] Quadrio, M., Floryan, J. M., and Luchini, P., "Effect of streamwise-periodic wall transpiration on turbulent friction drag," *Journal of Fluid Mechanics*, Vol. 576, 2007, pp. 425–444. https://doi.org/10.1017/S0022112007004727.

[29] Mamori, H., and Fukagata, K., "Drag reduction effect by a wave-like wall-normal body force in a turbulent channel flow," *Physics of Fluids*, Vol. 26, No. 11, 2014, pp. 1–23. https://doi.org/10.1063/1.4901186.

[30] Lozano-Durán, A., and Jiménez, J., "Effect of the computational domain on direct simulations of turbulent channels up to Re_τ = 4200," *Physics of Fluids*, Vol. 26, No. 1, 2014, pp. 1–7. https://doi.org/10.1063/1.4862918.

[31] Ibrahim, J. I., Gómez-de Segura, G., Chung, D., and García-Mayoral, R., "The smooth-wall-like behaviour of turbulence over drag-altering surfaces: a unifying virtual-origin framework," *Journal of Fluid Mechanics*, Vol. 915, 2021, p. A56. https://doi.org/10.1017/jfm.2021.13.

[32] Lee, M., and Moser, R. D., "Direct numerical simulation of turbulent channel flow up to $\mathrm{Re}_\tau \approx 5200$," *Journal of Fluid Mechanics*, Vol. 774, 2015, pp. 395–415. https://doi.org/10.1017/jfm.2015.268.

[33] Modesti, D., Endrikat, S., Hutchins, N., and Chung, D., "Dispersive stresses in turbulent flow over riblets," *Journal of Fluid Mechanics*, Vol. 917, 2021. https://doi.org/10.1017/jfm.2021.310.

[34] Lee, S., Ayton, L. J., Bertagnolio, F., Moreau, S., Chong, T. P., and Joseph, P. F., "Turbulent boundary layer trailing-edge noise: Theory, computation, experiment, and application," *Progress in Aerospace Sciences*, Vol. 126, No. May, 2021, p. 100737. https://doi.org/10.1016/j.paerosci.2021.100737.

[35] Yakhina, G., Roger, M., Moreau, S., Nguyen, L., and Golubev, V., "Experimental and Analytical Investigation of the Tonal Trailing-Edge Noise Radiated by Low Reynolds Number Aerofoils," *Acoustics*, Vol. 2, No. 2, 2020, pp. 293–329. https://doi.org/10.3390/acoustics2020018.

[36] Nikuradse, J., "Laws of flow in rough pipes," *NACA Technical Report*, , No. 5, 1950, pp. 738–757. https://doi.org/10.1051/lhb/1951058.